
1 This manuscript is a preprint and has been submitted for publication in Terra Nova. Please note
2 that the manuscript has not been to be formally accepted for publication, and is currently under
3 review. Subsequent versions of this manuscript may have slightly different content. If accepted,
4 the final version of this manuscript will be available via the 'Peer-reviewed Publication DOI' link
5 on the right-hand side of this webpage. Please feel free to contact any of the authors; we
6 welcome feedback.

7

8

9 Brittle basement deformation during the Caledonian Orogeny
10 observed by K-Ar geochronology of illite-bearing fault gouge in
11 west-central Sweden

12 Bjarne Almqvist¹, Roelant van der Lelij², Karin Högdahl¹, Rodolphe Lescoutre¹, Jasmin
13 Schönenberger², Haakon Fossen³, Håkan Sjöström¹, Christopher Juhlin¹, Stefan Luth⁴, Susanne
14 Grigull^{4,5}, Giulio Viola⁶

15 1. Uppsala University, Department of Earth Sciences, Villavägen 16, 752 36, Uppsala, Sweden
16 (*bjarne.almqvist@geo.uu.se*)

17 2. Geological Survey of Norway, Leiv Eirikssons vei 39, 7040, Trondheim, Norway

18 3. University of Bergen, Museum of Natural History, Allégaten 41, 5007 Bergen, Norway

19 4. Geological Survey of Sweden, Villavägen 18, 752 36, Uppsala, Sweden

20 5. Svensk Kärnbränslehantering AB (SKB), Evenemangsgatan 13, 169 03, Solna, Sweden

21 6. University of Bologna, Department of Biological, Geological and Environmental Sciences,
22 Via Zamboni 67, Bologna

23

24 Submitted to: *Terra Nova*

25 Short title (running head):

26 Basement faulting during the Caledonian orogeny

27 Statement of significance:

28 We present the first K-Ar geochronology ages from fault gouge in the crystalline basement of
29 central-western Sweden, where brittle deformation localizes in and along pre-existing mafic
30 intrusions that intruded granite host rocks. The ages indicate that the basement was deformed
31 during the Caledonian orogeny in central Scandinavia. Caledonian intrusion-guided basement
32 deformation may be widespread, as is indicated by out chronological results in combination with
33 geophysical observations (Lescoutre et al., 2022) and deep drilling (Lorenz et al., 2022).

34 **Abstract**

35 This study presents K-Ar geochronology ages of illite from fault gouge in the crystalline
36 basement in central-western Sweden. Samples of fault gouge were taken from two faults
37 localizing brittle deformation along and within mafic dikes that intrude Paleoproterozoic
38 granites. K-Ar ages from the ten dated fractions span from 823 Ma to 392 Ma. The older ages
39 obtained, spanning from 823 to 477 Ma, are influenced by a mixture of illite and K-feldspar, the
40 latter which likely formed during a hydrothermal event prior to faulting. The remaining ages are
41 obtained from fractions hosting only authigenically formed illite. The illite dominated gouge,
42 from both faults, show that illite crystallized during the Caledonian orogeny, with a range in ages
43 from 442.1 ± 9.7 to 391.7 ± 6.1 Ma. These results indicate that basement likely played a significant
44 role in continental contraction during the Caledonian Orogeny, influencing both the mode and
45 penetration of deformation into the continent.

46

47 Keywords: Scandinavian Caledonides, K-Ar geochronology, Faulting, (Baltica) basement, brittle
48 deformation

49

50

51 **1. Introduction**

52 Cratonic nuclei are generally considered stable for billions of years and make up the cores of
53 continents. There is, however, limited understanding regarding their brittle structural evolution
54 and deformation history (e.g., Tillberg et al., 2020; 2021). Studies of exposed faults in
55 continental interiors provide the possibility to understand how brittle deformation affects
56 continent interiors. Such deformation can, for example, result from far-field stresses that were
57 generated at plate boundaries during orogeny (van der Pluijm et al., 1997; Pinet, 2015;

58 Goodfellow et al., 2017). The overall style of deformation during orogeny generally depends on
59 the position in the orogen (Fossen, 2016). Whereas the collision zone is commonly characterized
60 by pervasive, medium- to high-grade ductile deformation, the foreland and plate interiors
61 (basement) are generally deformed through colder, more brittle structures, and low-grade
62 metamorphism, if any. It is challenging to assess the relative involvement of the foreland and
63 plate interior basement and its role in orogeny. Structural inheritance and reactivation further
64 complicate localization, timing and distribution of deformation within orogenic foreland domains
65 via the formation of multiple decoupling levels in the crust or reactivation of pre-existing weak
66 faults or structures (e.g., Lacombe and Mouthereau, 2002; Mattila and Viola, 2014).

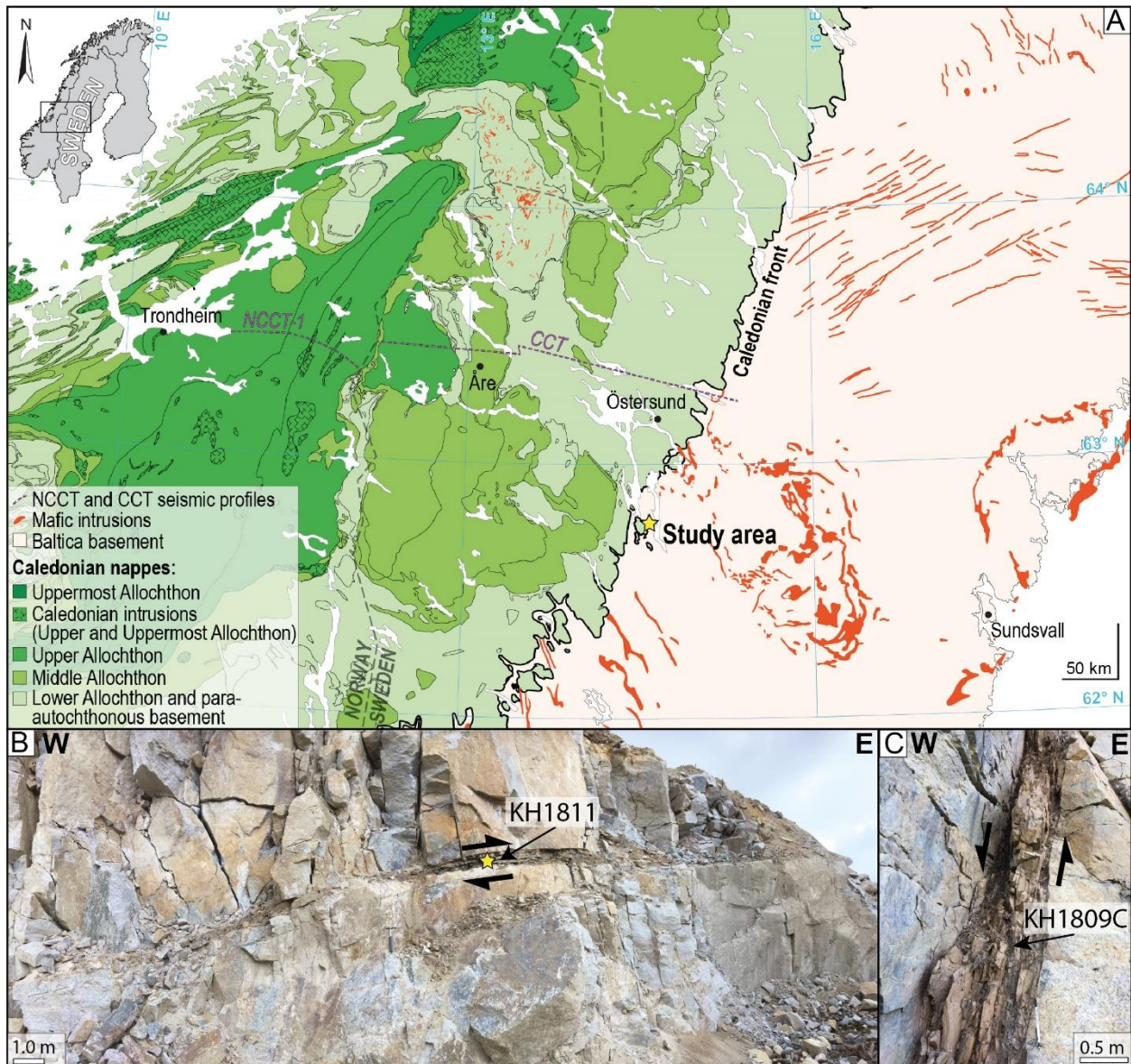
67 The Scandinavian Caledonides represent a well-exposed, deeply eroded Paleozoic orogen. It has
68 been compared in size and structure to present-day Himalayas (Gee et al., 2010; Labrousse et al.,
69 2010; Streule et al., 2010). Key questions concerning the Scandinavian Caledonides are how
70 deformation was distributed in space and through time during the evolution of the orogen, and
71 what role pre-existing structures played in shaping its architecture. In its external part, Cambrian
72 shales acted as a major décollement level along which deformation localized during the eastward
73 transport of the overlying allochthonous nappes (e.g., Gee, 1978; Rice and Anderson, 2016).
74 However, seismic reflection imaging across the central Scandinavian Caledonides shows a
75 pervasively reflective upper crust, down to at least 15 km present depth, which is characterized
76 by sub-horizontal and west-dipping reflectors (Palm et al., 1994; Hurich et al., 1989; Juhojuntti
77 et al., 2001; Juhlin et al., 2016). These reflectors are intriguing because they occur well below
78 the shale décollement and recent scientific deep drilling have confirmed that reflections are
79 likely to originate from mafic intrusions (Lorenz et al., 2022).

80 Here, we focus on a sequence of brittle faulting events within the basement of Baltica in central
81 Sweden, near the present-day Caledonian orogenic front. Two samples of fault gouge were
82 processed and dated by K-Ar geochronology to produce absolute time constraints on the local
83 faulting history. The obtained ages span the Cryogenian-Ediacaran time interval to the Devonian.
84 In particular, our results show that the crystalline basement experienced brittle faulting at
85 discrete times during the Caledonian Orogeny.

86

87 **2. Geological Setting**

88 The crystalline basement east of the present-day location of the Caledonian front is dominated by
89 Svecof Karelian, 1.88 to 1.74 Ga granitoids (Fig. 1a; Fig. S1). We studied two faults (Fig. 1b, c)
90 located less than 10 km from the Caledonian front, within these granitoids. The faulting localized
91 mainly along and within dolerite dikes that have intruded into the granite (Fig. 1b, c). These
92 dikes belong to the ca. 1250 Ma Central Scandinavian Dolerite Group (CSDG; Gorbatshev et
93 al., 1979; Söderlund et al., 2006). Similar dolerite intrusions are common throughout the region
94 and range in thickness from ~0.5 m to >1 km, with a prevalent NNW-SSE strike (Fig. S1).
95 Undeformed CSDG dikes east of the Caledonian front are mainly composed of unaltered
96 plagioclase, clinopyroxene and altered orthopyroxene (Fig. S2a-d).



97

98 Figure 1. (A) Map of the Baltica basement and the main tectonic units of the central Scandinavian
 99 Caledonides (modified from Robinson et al. 2014); CSDG mafic dikes are shown in red (based on
 100 databases from the Geological Survey of Sweden). The CCT and NCCT-1 seismic profiles across the
 101 central Scandinavian Caledonides are indicated by the dashed purple line (see Fig. 3); (B, C) Field
 102 pictures of the faulted dikes hosted by granite. (B) Low-angle west-dipping thrust fault showing brittle
 103 deformation localized along a ca. 0.4 m thick dolerite dike with sample location of KH1811; (C) Steeply
 104 oriented, west-dipping fault with inferred west side down movement with sample location of KH1809C.

105

106 Samples KH1811 and KH1809C were collected from a W-NW shallow-dipping fault and from a
107 steeply west-dipping fault, respectively, which have nucleated along and within mafic intrusions
108 (Fig. 1b, c). The shallow-dipping mafic intrusion has a thickness of ca. 0.4 m, but a similar sub-
109 parallel dike nearby has a thickness up to several meters. Top-to-the southeast thrusting along
110 this intrusion is constrained by Riedel shears and thin shear bands observed in the host granite, as
111 well as shear sense indicators in thin sections (Fig. S2e, f). For the steeply oriented faulted dike a
112 dominant west-down (normal) sense movement is inferred based on the orientation of the fault
113 and diffuse shear bands.

114

115 **3. Methodology**

116 **3.1 Sample preparation**

117 The bulk samples were submerged in deionized water and gently disaggregated using repeated
118 (>100) freeze-thaw cycles. Size fractions of <0.1 μm , 0.1-0.4 μm , 0.4-2 μm , 2-6 μm and 6-10 μm
119 were then generated using a combination of gravity settling in cylinders for the isolation of the
120 >2 μm fractions, and continuous flow centrifugation for generation of the fractions <2 μm . The
121 generated fractions were collected with a high-speed fixed angle centrifuge and dried in an oven
122 at 50 °C.

123

124 **3.2 X-ray diffraction and K-Ar dating of clay mineral fraction**

125 The mineralogical composition of all grain size fractions was studied with X-ray diffraction
126 (XRD). Randomly-oriented samples were prepared by side-loading and analyzed with a Bruker
127 D8 Advance X-ray diffractometer operating with a Cu X-ray tube (40 kV/40 mA) and Lynxeye
128 XE detector. Mineral quantification was performed on randomly prepared specimens using
129 Rietveld modeling with the TOPAS 5 software. Illite crystallinity (Kübler Index) was determined
130 from the full-width at half maximum (FWHM) of the 10 Å peak and standardized according to
131 Warr (2018) and Warr & Rice (1994).

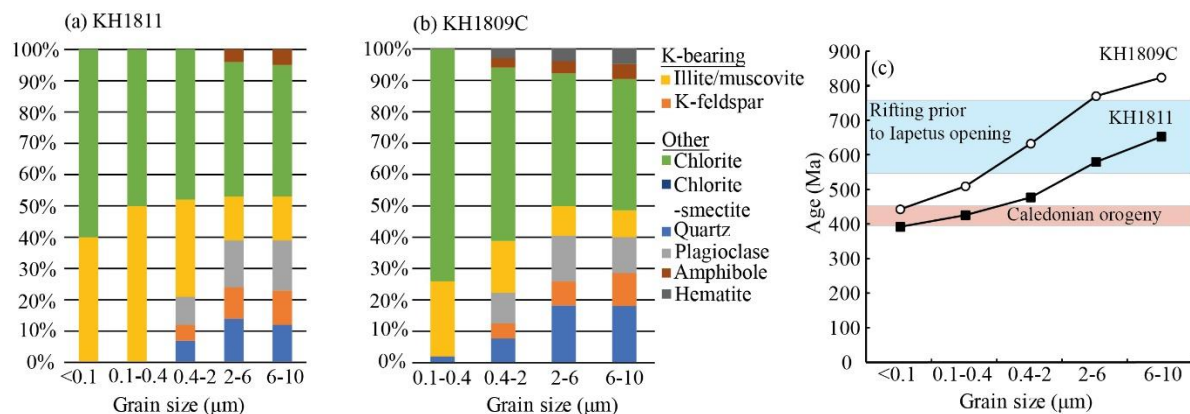
132 The homogenized clay materials and standards were packed in weighted molybdenum envelopes.
133 Argon isotopes were determined on an IsotopX NGX multicollector noble gas mass spectrometer
134 using faraday cups fitted with $10^{12} \Omega$ amplifiers, except for ^{40}Ar , which was measured using a
135 faraday cup fitted with a $10^{11} \Omega$ amplifier. Potassium concentrations were determined by
136 digesting aliquots of ~50 mg of sample material in $\text{Li}_2\text{B}_4\text{O}_7$ flux at a temperature of $1000 \pm 50 \text{ }^\circ\text{C}$
137 in palladium crucibles. The resulting glass was subsequently dissolved in HNO_3 , and analyzed
138 on a Perkin Elmer Optima 4300 DV ICP-OES. 1σ uncertainties depend on the sample weight and
139 its K concentration, and are better than 1.5% relative for pure illite/mica, as determined by
140 repeated measurements of several geological standards. K-Ar ages were calculated using the ^{40}K
141 decay constants, abundance and branching ratio of Steiger and Jaeger (1977). Atmospheric argon
142 corrections were performed using the relative abundances of ^{40}Ar , ^{38}Ar and ^{36}Ar of Lee et al.
143 (2006; $^{40}\text{Ar}/^{36}\text{Ar} = 298.56 \pm 0.31$). Further details on the XRD and K-Ar analyses are given in the
144 supplementary material.

145

146 **4. Results**

147 **4.1 X-ray diffraction and sample mineral composition**

148 The samples are characterized by similar mineralogical composition and concentrations of clay
 149 minerals (Fig. 2a, b; supplementary Table S1, Fig. S3). The separated fine fractions consist
 150 mainly of chlorite + smectite and illite/muscovite, with lesser amounts of quartz, K-feldspar and
 151 plagioclase, and minor amounts of amphibole and hematite. Quartz and feldspar are more
 152 abundant in the coarse grain fractions, whereas they are nearly absent in the <0.1 and 0.1-0.4 μm
 153 fractions. The illite/muscovite concentration is higher in KH1811. The 1M polytype is the sole
 154 type of illite identified in the fine grain fractions, ranging from <0.1 μm up to 2 μm . In sample
 155 KH1809C, there are indications that the 2M₁ illite polytype is also present in the 2-6 μm and 6-
 156 10 μm grain-size fractions. In these two fractions, the 10 Å peaks are well defined and the typical
 157 2M₁ peak at 2.8 Å is clearly visible.



158
 159 Figure 2. (a, b) Mineral modal composition from XRD for samples KH1811 and KH1809C. Note that the
 160 finest fraction (<0.1 μm) did not yield a discernable modal composition from XRD in sample KH1809C;
 161 (c) K-Ar geochronology results as a function of the separated clay mineral grain-size fraction (1 σ
 162 standard deviation are smaller than the symbol representing the data point).

163

164 **4.2 K-Ar geochronology**

165 The K-Ar results are summarized in Table 1 and shown in Figure 2C. Sample KH1809C shows a
 166 distribution of ages that range from 822.7±11.6 Ma to 442.1±9.7 Ma, whereas KH1811 shows a
 167 narrower distribution of ages, ranging from 652.2±8.9 Ma to 391.7±6.1 Ma (Fig. 2c; Table 1).
 168 The coarser grain-size fractions invariably yield older ages, whereas the finest grain-size
 169 fractions yield the youngest ages. Sample KH1809C yielded older ages than KH1811, for all
 170 dated grain size fractions. It can be noted that the K-feldspar to illite ratio is higher for all grain-
 171 size fractions of KH1809C.

Sample parameters		⁴⁰ Ar				K			Age data	
Sample name	Fraction (µm)	Mass mg	mol/g	σ (%)	⁴⁰ Ar* %	Mass mg	wt %	σ (%)	Age (Ma)	σ (±Ma)
KH1811	<0.1	1.578	2.423E-09	0.34	90.8	14.6	3.193	1.69	391.7	6.1
	0.1-0.4	1.470	3.020E-09	0.35	93.5	49.9	3.631	1.41	425.3	5.5
	0.4-2	1.702	2.792E-09	0.33	94.0	49.9	2.951	1.51	476.7	6.5
	2-6	1.848	2.815E-09	0.31	94.4	50.9	2.377	1.59	579.0	8.0
	6-10	1.636	3.281E-09	0.33	94.0	50.1	2.408	1.60	652.2	8.9
KH1809C	<0.1	1.022	1.046E-09	0.48	90.3	17.4	1.204	2.44	442.1	9.7
	0.1-0.4	1.266	1.708E-09	0.40	93.5	50.0	1.676	1.76	508.6	8.0
	0.4-2	1.860	2.178E-09	0.31	95.8	50.1	1.660	1.76	632.0	9.5
	2-6	3.374	2.869E-09	0.25	97.3	50.0	1.725	1.75	769.3	11.1
	6-10	1.896	3.218E-09	0.31	97.8	50.0	1.780	1.73	822.7	11.6

172
 173 Table 1. Summary of K-Ar geochronology results.

174

175 5. Discussion and conclusions

176 5.1 Origin of the clay mineral fraction in the faulted dikes

177 It is important to assess whether illite formed authigenically during faulting or whether it is at
 178 least in part protolithic or related to other geological events that are not necessarily tied to
 179 deformation (e.g., a hydrothermal alteration event). Sample KH1811 lacks the typical 2M₁
 180 polytype peak at 2.8 Å, implying that this sample exclusively contains the 1M polytype. In
 181 contrast, the presence of 2M₁ polytype illite/muscovite in the two coarsest grain size fractions of
 182 sample KH1809C, as shown by the well-defined peak at 10 Å and the presence of the 2.8 Å

183 peak, implies that these fractions contain illite/muscovite of a potentially inherited origin.
184 Alternatively, the $2M_1$ polytype may have originated from hydrothermal fluids or faulting at
185 higher temperatures. Notably, the coarser grain size fractions contain up to 10 vol% K-feldspar,
186 which is likely to have an influence on the ages of the coarser fractions where K-feldspar
187 concentration is comparable to that of illite. The K-feldspar appears to originate during an earlier
188 hydrothermal event (Fig. S2g, h; Table S2). The finest grain size fractions, 0.1-0.4 μm fraction
189 for sample KH1809C and the $<0.1 \mu\text{m}$ and 0.1-0.4 μm fractions for sample KH1811, are
190 interpreted to have formed authigenically during faulting because of the predominance of the 1M
191 illite polytype and absence of K-feldspar. As such they are interpreted as to represent the timing
192 of slip events that took place along the sampled faults, according to the age attractor model of
193 Torgersen et al. (2014; 2015) and Viola et al. (2016). Note that a very small fraction of K-
194 feldspar ($<1 \%$) can be present in the fine-grained samples, arising from the limit of detection
195 with XRD. However, the presence of up to 1 % of hydrothermal origin K-feldspar in the most
196 fine-grained portions of samples, with a maximum age of $\sim 1250 \text{ Ma}$, would skew the resultant
197 ages less than 10 Ma. This suggests that a non-detectible fraction of K-feldspar, from XRD
198 measurements, would contribute very little to the observed ages and the presence of K-feldspar is
199 not responsible for differences in ages observed for the most fine-grained fractions in either
200 sample.

201

202 **5.2 Brittle deformation in the Baltica basement during Caledonian orogeny**

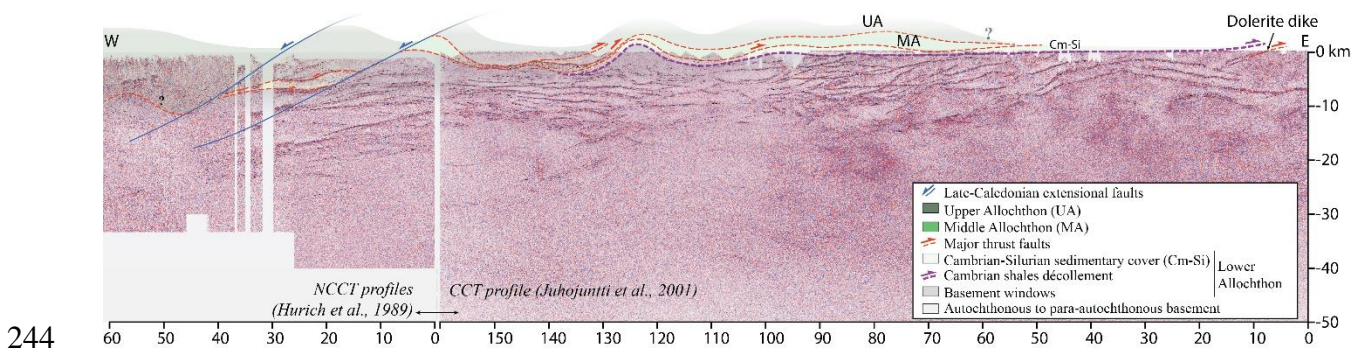
203 The oldest ages observed in both samples show a portion of K-feldspar mixed with illite, likely
204 originating from hydrothermal fluids. In contrast, the youngest ages from 442 Ma to 392 Ma
205 result from a single source of the 1M illite polytype and indicate Caledonian signatures where

206 faulting occurs prior to and during continent-continent collision. The limitation of the current
207 data set is recognized, in terms of the limited number of samples (two samples with 10 size
208 fractions) and the possibility for mixed ages in the separated grain-size fractions. A mixture of
209 ages is suggested by the absence of a plateau in the ages presented in Figure 2 (i.e., inclined age
210 spectra). However, the K-Ar ages show small standard deviations, which indicate limited mixing
211 of K-Ar ages within the same grain-size fraction. Furthermore, samples from both faults
212 demonstrate that Caledonian age fault movement took place in the basement rocks. This latter
213 point indicates that the Baltica basement accommodated brittle deformation during the
214 Caledonian orogeny, which is the first time this has been established by geochronology on the
215 foreland side of the Scandinavian Caledonides.

216 The youngest ages are recorded in the gouge of the shallow W-dipping fault (KH1811), where a
217 top SE thrust sense of movement is inferred. The older age of ~442 Ma pre-dates the continent-
218 continent collision of Baltica and Laurentia, and is found on the steep, apparent normal, W-
219 dipping fault (KH1809C). This age would correspond to localized high-grade and high-pressure
220 metamorphism of subducted continental crust in the central Scandinavian Caledonides and
221 slightly predates widespread magmatic activity (440-430 Ma) along the entire orogen (Slagstad
222 and Kirkland, 2018). How then did the deformation front reach the sample localities far into
223 Sweden already at the dawn of the Silurian, at ~442 Ma? One explanation is that stresses were
224 transmitted far east because of a cold and rigid basement during closure of the Iapetus Ocean and
225 initial continental collision (e.g., Fossen et al., 2017), which would physically manifest through
226 faulting of the Baltica basement.

227 Strain localization along and within dikes may have been important during deformation of the
228 Baltica basement. The generally west-dipping structures observed in the eastern parts of the CCT

229 seismic profile (Juhojuntti et al., 2001) are in a favorable position to accommodate strain and be
 230 (re)activated (Fig. 3). The reflection seismic images indicate that the CSDG dikes are distributed
 231 in the basement, at least, in and east of the Caledonian front and have been inferred to occur,
 232 based on geochemistry, as far west as the Tømerrås basement window in Norway (Johansson,
 233 1980). Greiling et al. (2007) have noted a progressive increase in faulting and deformation,
 234 involving the CSDG intrusions, from the exterior to the interior of the orogen. Importantly, they
 235 noted a striking rheological contrast between dikes and the granitic basement, where the former
 236 is considerably less competent at low grade metamorphic conditions. In our study area the dikes
 237 never experienced deformation at high grade conditions, and the rheological contrast between
 238 dike and host rock is the likely reason for localization along dikes (e.g., Wilson et al., 2020).
 239 Recently, Lescoutre et al. (2022) indicate that shortening took place in the basement underneath
 240 the allochthonous cover, where mafic sheets likely guided the contractional deformation. Partial
 241 kinematic restoration of Lescoutre et al. (2022), based on seismic reflection profiles, provide a
 242 minimum displacement of ~6 km, along one restoration plane in the crystalline basement, and
 243 displacements in the basement are likely to be significantly larger.



245 Figure 3: Seismic reflection profiles CCT and the eastern part of NCCT-1 (shown in Fig. 1), with a
 246 simplified interpretation of the main tectonic units in the uppermost crust and outlined prominent seismic
 247 reflectors in the basement. Prominent seismic reflections are present throughout the basement in the upper

248 10-15 km, although they change in character from east to west. Note surface exposed dolerite intrusion at
249 eastern margin of the profile.

250

251 The observations and geochronology results presented here can be used to draw three
252 conclusions. First, the crystalline basement of Baltica was involved in deformation related to the
253 Caledonian Orogeny. The results presented in this study provides the first direct evidence in
254 central Scandinavia for brittle deformation, through faulting and determination of the age of the
255 fault events. Second, any estimate of continental contraction must therefore include deformation
256 in the foreland and crystalline basement, and not only in allochthonous units and along the
257 décollement. Such a case has recently been illustrated by Duvall et al. (2020), who showed that
258 blind faults occurring in the Indian basement, south of the Himalayan Main Frontal Thrust, likely
259 lead to an underestimation of the collisional convergence and rate of convergence. Third, the
260 accommodation of deformation in the basement far away from the collision zone indicates that
261 stress is transmitted into the craton from the collision zone. Van der Pluijm et al. (1997) have
262 indicated that mountain belts are in fact “filters” of stress and that the specific style and
263 properties of convergence are not reflected in the stress state of continental interiors. Differential
264 stresses generated by orogeny at the collision zone, on the order to ~20 MPa, could transmit
265 several thousand kilometers into the continents. These stresses could then be responsible for (re-
266)activation and failure of favorably oriented structures, for example along pre-existing faults, but
267 also along and in sills and dikes, such as exists near and underneath the Caledonian foreland in
268 the crystalline basement of Baltica.

269

270

271 **Acknowledgements**

272 This study was made possible through financial support of the Swedish Geological Survey, grant
273 36-1940/2017. X. Ruikai Xie at NGU laboratory is thanked for careful K analysis.

274

275 **References cited**

276 Bender, H., Glodny, J., and Ring, U., 2019, Absolute timing of Caledonian orogenic wedge
277 assembly, Central Sweden, constrained by Rb-Sr multi-mineral isochron data: *Lithos*, v. 344-
278 345, p. 339-359.

279 Duvall, M.J., Waldron, J.W.F., Godin, L., and Najman, Y., 2020, Active strike-slip faults and an
280 outer frontal thrust in the Himalayan foreland basin: *Proceedings in the National Academy of*
281 *Sciences*, v. 117, p. 17615-17621.

282 Fossen, H., 2016, *Structural Geology*, 2nd ed.: New York, Cambridge University Press, 524 pp.

283 Fossen, H., and Dunlap, W. J., 1998, Timing and kinematics of Caledonian thrusting and
284 extensional collapse, southern Norway: evidence from ⁴⁰Ar/³⁹Ar thermochronology: *Journal of*
285 *Structural Geology*, v. 20, p. 765-781.

286 Fossen, H., Cavalcante, G.C., and Paes de Azevedo, R., 2017, Hot versus cold orogenic behavior:
287 Comparing the Araçuaí-West Congo and the Caledonian orogens: *Tectonics*, v. 36, p. 2159-
288 2178.

289 Gee, D., 1978, Nappe displacement in the Scandinavian Caledonides: *Tectonophysics*, v. 47, p.
290 393-394.

291 Gee, D.G., Juhlin, C., Pascal, C., and Robinson, P., 2010, Collisional Orogeny in the
292 Scandinavian Caledonides (COSC): *Geologiska Föreningen i Stockholm Förhandlingar*, v. 132,
293 p. 29-44.

294 Goodfellow, B.W., Viola, G., Bingen, B., Nuriel, P., and Kylander-Clark, A.R.C., 2017,
295 Paleocene faulting in SE Sweden from U-Pb dating of slickenfibres calcite: *Terra Nova*,
296 doi:10.1111/ter.12280.

297 Gorbatshev, R., Solyom, Z., and Johansson, I., 1979, The Central Scandinavian Dolerite Group
298 in Jämtland, central Sweden: *Geologiska Föreningen i Stockholm Förhandlingar*, v. 101, p. 177-
299 190.

300 Grathoff, G., and Moore, D.M., 1996, Illite Polytype Quantification using WILDFIRE©
301 Calculated X-Ray Diffraction Patterns: *Clays and Clay Minerals*, v. 44 (6), p. 835-842.

302 Greiling, R.O., Grimmer, J.C., De Wall, H., and Björk, L., 2007, Mesoproterozoic dyke swarms
303 in foreland and nappes of the central Scandinavian Caledonides: structure, magnetic fabric, and
304 geochemistry: *Geological Magazine*, v. 144, p. 525-546.

305 Hurich, C.A., Palm, H., Dyrelus, D., and Kristoffersen, Y., 1989, Deformation of the Baltic
306 continental crust during Caledonide intracontinental subduction: Views from seismic reflection
307 data: *Geology*, v. 17, p. 423-425.

308 Johansson, L., 1980, Petrochemistry and regional tectonic significance of metabasites in
309 basement windows of the central Scandinavian Caledonides: *Geologiska Föreningen i Stockholm*
310 *Förhandlingar*, v. 102, p. 499-514.

311 Juhlin, C., Hedin, P., Gee, D.G., Lorenz, H., Kalscheuer, T., and Yan, P., 2016, Seismic imaging
312 on the eastern Scandinavian Caledonides: siting the 2.5 km deep COSC-2 borehole, central
313 Sweden: *Solid Earth*, v. 7, p. 769-787.

314 Juhojuntti, N., Juhlin, C., and Dyrelus, D., 2001, Crustal reflectivity underneath the Central
315 Scandinavian Caledonides: *Tectonophysics*, v. 334, p. 191-210.

316 Labrousse, L., Hetényi, G., Raimbourg, H., Jolivet, L., and Andersen, T.B., 2010, Initiation of
317 crystal-scale thrusts triggered by metamorphic reactions at depth: Insights from a comparison
318 between the Himalayas and Scandinavian Caledonides: *Tectonics*, v. 29(5),
319 doi:10.1029/2009TC002602.

320 Lacombe, O., and Mouthereau, F., 2002, Basement-involved shortening and deep detachment
321 tectonics in forelands of orogens: Insights from recent collision belts (Taiwan, Western Alps,
322 Pyrenees): *Tectonics*, v. 21, doi:10.1029/2001TC9010118.

323 Lee, J.-Y., Marti, K., Severinghaus, J.P., Kawamura, K., Yoo, H.-S., Lee, J.B., and Kim, J.S.,
324 2006, A redetermination of the isotopic abundances of atmospheric Ar: *Geochimica et*
325 *Cosmochimica Acta*, v. 70, p. 4507–4512.

326 Lescoutre, R., Almqvist, B., Koyi, H., Berthet, T., Hedin, P., Galland, O., Brahimi, S., Lorenz,
327 H., Juhlin, C., 2022, Large-scale flat-lying mafic intrusions in the Baltican crust and their
328 influence on basement deformation during the Caledonian orogeny: *GSA Bulletin*,
329 <http://doi.org/10.1130/B36202.1>.

330 Lorenz, H., Rosberg, J.-E., Juhlin, C., Klonowska, I., Lescoutre, R., Westmeijer, G., Almqvist,
331 B.S.G., Anderson, M., Bertilsson, S., Dopson, M., Kallmeyer, J., Kück, J., Lehnert, O.,

332 Menegon, L., Pascal, C., Rejkjær, S., Roberts, N.N.W., 2022, COSC-2 – drilling the basal
333 décollement and underlying margin of paleocontinent Baltica in the Paleozoic Caledonide
334 Orogen of Scandinavia: *Scientific Drilling*, 30, 43-57.

335 Mattila, J., and Viola, J., 2014, New constraints on 1.7 Gyr of brittle tectonic evolution in
336 southwestern Finland derived from a structural study at the site of a potential nuclear waste
337 repository (Olkiluoto Island): *Journal of Structural Geology*, v. 67, p. 50-74.

338 Palm, H., Gee, D., Dyrelius, D., and Björklund, L., 1991, A reflection seismic image of
339 Caledonian structure in Central Sweden: Geological Survey of Sweden report, Ca 75.

340 Pinet, N., 2015, Far-field effects of Appalachian orogenesis: A view from the craton: *Geology*, v.
341 44, p. 83-86.

342 Rice, A.H.N., and Anderson, M.W., 2016, Restoration of the external Scandinavian Caledonides:
343 *Geological Magazine*, v. 153, p. 1136-1165.

344 Robinson, P., Roberts, D., Gee, D. G., and Solli, A., 2014, A major synmetamorphic Early
345 Devonian thrust and extensional fault system in the Mid Norway Caledonides: relevance to
346 exhumation of HP and UHP rocks: Geological Society, London, Special Publications, v. 390(1),
347 p. 241–270.

348 Slagstad, T., and Kirkland, C.L., 2018, Timing of collision initiation and location of the Scandian
349 orogenic suture in the Scandinavian Caledonides: *Terra Nova*, v. 30, p. 179-188.

350 Söderlund, U., Elming, S.-Å., Ernst, R.E., and Schissel, D., 2006, The Central Scandinavian
351 Dolerite Group – Protracted hotspot activity or back-arc magmatism? Constraints from U-Pb
352 baddeleyite geochronology and Hf isotopic data: *Precambrian Research*, v. 150, p. 136-152.

353 Steiger, R.H., and Jäger, E., 1977, Subcommittee on geochronology: convention on the use of
354 decay constants in geochronology and cosmochronology: *Earth and Planetary Science Letters*, v.
355 36, p. 359–362.

356 Streule, M.J., Strachan, R.A., Searle, M.P., and Law, R.D., 2010, Comparing Tibet-Himalayan and
357 Caledonian crustal architecture, evolution and mountain building processes: Geological Society,
358 London, Special Publications, v. 335, p. 207-232.

359 Tillberg, M., Drake, H. Zack, T., Kooijman, E., Whitehouse, M.J., and Åström, M.E., 2020, In
360 situ Rb-Sr dating of slickenfibres in deep crystalline basement faults: *Nature Scientific Reports*,
361 v. 10:562, doi:10.1038/s41598-019-57262-5.

362 Tillberg, M., Drake, H., Zack, T., Hogmalm, J., Kooijman, E., Åström, M., 2021, Reconstructing
363 craton-scale tectonic events via in situ Rb-Sr geochronology of poly-phased vein mineralization:
364 *Terra Nova*, v.33, 502-510, doi:10.1111/ter.12542.

365 Torgersen, E., Viola, G., Zwingmann, H., Harris, C., 2014, Structural and temporal evolution of
366 a reactivated brittle-ductile fault – Part II: Timing of fault initiation and reactivation by K-Ar
367 dating of synkinematic illite/muscovite: *Earth Planet. Sci. Lett.*, v.407, 221-233.

368 Torgersen, E., Viola, G., Zwingmann, H., and Henderson, I.H., 2015, Inclined K-Ar age spectra
369 in brittle fault gouges: effects of fault reactivation and wall-rock contamination: *Terra Nova*, v.
370 27, p. 106-113, doi:10.1111/ter.12136.

371 Van der Pluijm, B., Craddock, J.P., Graham, B.R., and Harris, J.H., 1997, Paleostress in Cratonic
372 North America: Implications for Deformation of Continental Interiors: *Science*, v. 277, p. 794-
373 796.

374 Viola, G., Scheiber, T., Fredin, O., Zwingmann, H., Margreth, A., and Knies, J., 2016,
375 Deconvoluting complex structural histories archived in brittle fault zones: *Nature*
376 *Communications*, v. 7, 13448, doi:10.1038/ncomms13448.

377 Warr, L.N., 2018, A new collection of clay mineral “Crystallinity” Index standards and revised
378 guidelines for the calibration of Kübler and Árkai indices: *Clay Minerals*, v. 53, p. 1-12.

379 Warr, L.N. and Rice, A.H.N., 1994, Interlaboratory standardization and calibration of clay
380 mineral crystallinity and crystallite size data: *Journal of metamorphic Geology*, v. 12, p. 141-
381 152.

382 Wilson, C.J.L., Vassallo, J.J., and Hoek, J.D., 2020, Rheological behaviour of mafic dykes
383 deformed in a granite host, Wanna, Eyre Peninsula, South Australia: *Journal of Structural*
384 *Geology*, v. 140, 104164.

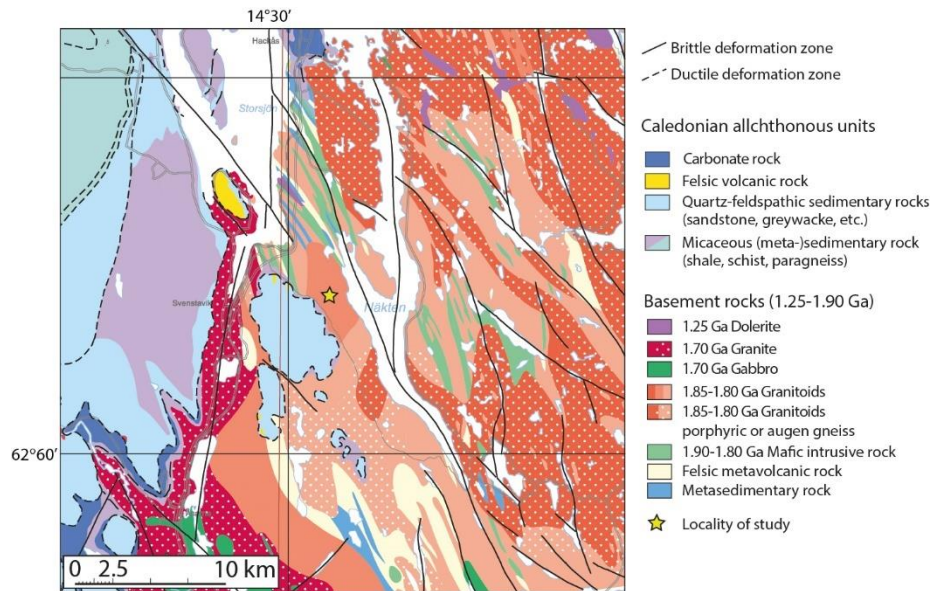
385

386 Electronic supplementary material

387

388 S.1 Geological setting and mineral composition of the CSDG mafic intrusions

389



390

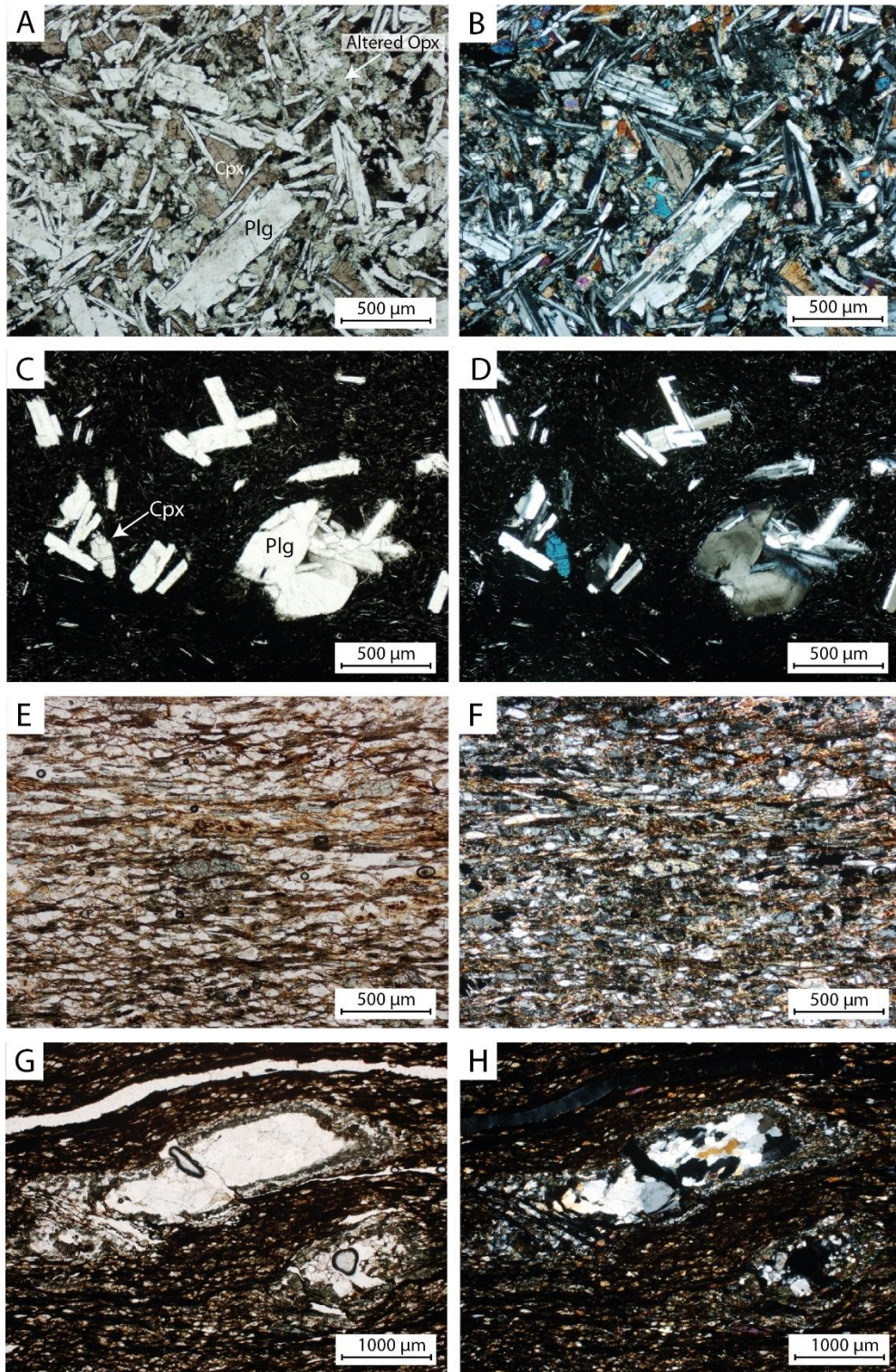
391 Figure S1. Details on the bedrock geology around the sampling locality. Note that the sampling

392 locality is situated in 1.80-1.85 granites, a few km east of the present-day Caledonian

393 allochthonous front (units in blue and purple color). The map has been created using the

394 Geological Survey of Sweden online map generator

395 (http://apps.sgu.se/kartgenerator/maporder_sv.html)



396

397 Figure S2. Microphotographs of (A-D) an undeformed CSDG dike at Hackås, ca. 10 km west of
 398 the study locality and (E-H) deformed dike from which sample KH1811 was collected. (A) and
 399 (B) is from inner part of the dike and (C) and (D) are from chilled margin near the dike wall
 400 contact; (A) and (C) images are taken in plane-polarized light and (B) and (D) images are taken
 401 in cross-polarized light. Note that the images were taken from samples from dikes that were

402 unaffected by brittle deformation (reflecting the composition and state of alteration of the
403 original CSDG dikes), and are located a few km away from the study locality. (E) and (F) thin
404 section images in plane polarized and cross polarized light, respectively, from deformed dike
405 (Fig. 1B), sample location KH1811. Secondary clay minerals are dominated by
406 chlorite/chloritoids and lesser amounts of other clay minerals, including illite. Adularia may be
407 present, as indicated by very low interference colors (Fig. S2F). (G-H) K-feldspar clast with clay
408 minerals surrounding it, showing a shear sense indicator with top to the SE kinematics.

409

410 S.2 Details on the sample analysis with X-ray diffraction and K-Ar dating

411

412

413 S2.1 X-ray diffraction methodology

414 The mineralogical composition of all grain size fractions was studied with X-ray diffraction
415 (XRD). Randomly-oriented samples were prepared by side-loading and analyzed with a Bruker
416 D8 Advance X-ray diffractometer operating with a Cu X-ray tube (40 kV/40 mA) and Lynxeye
417 XE detector. The XRD scan was performed from 3 to 75° 2 θ with a step size of 0.02° 2 θ , a
418 measurement time of 1 s per step, and rotation speed of 30 per minute. Fixed divergence had an
419 opening of 0.6 mm and primary and secondary soller slits were 2.5°. A knife edge was used to
420 reduce scatter radiation. Mineral identification was carried out with the automatic and/or manual
421 peak search-match function of Bruker's Diffrac.EVA V3.1 software. using both Crystallographic
422 Open Database (COD) as well as the PDF 4 Minerals database from the International Centre for
423 Diffraction Data (ICDD). For further clay minerals study, oriented mounts of fractions 2-6 μ m
424 were prepared by letting 1 ml of sample suspension dry out on a glass slide. These slides were
425 measured at room temperature, after treatment with ethylene glycol for 24 h, and after heating at
426 550°C for 1 h.

427 Mineral quantification was performed on randomly prepared specimens using Rietveld modeling
428 with TOPAS 5 software. Refined parameters included crystallite size, unit cell dimensions, sample
429 displacement, preferred orientation as well as background coefficients. The lower detection limits
430 are mineral-dependent and estimated to be 1-2 wt% with an approximate uncertainty for the
431 Rietveld modeling (i.e., quantification) of at least 2-3 wt%.

432 Illite crystallinity (Kübler Index) was determined from the full-width at half maximum (FWHM)
433 of the 10 Å peak and standardized according to Warr (2018) and Warr & Rice (1994).

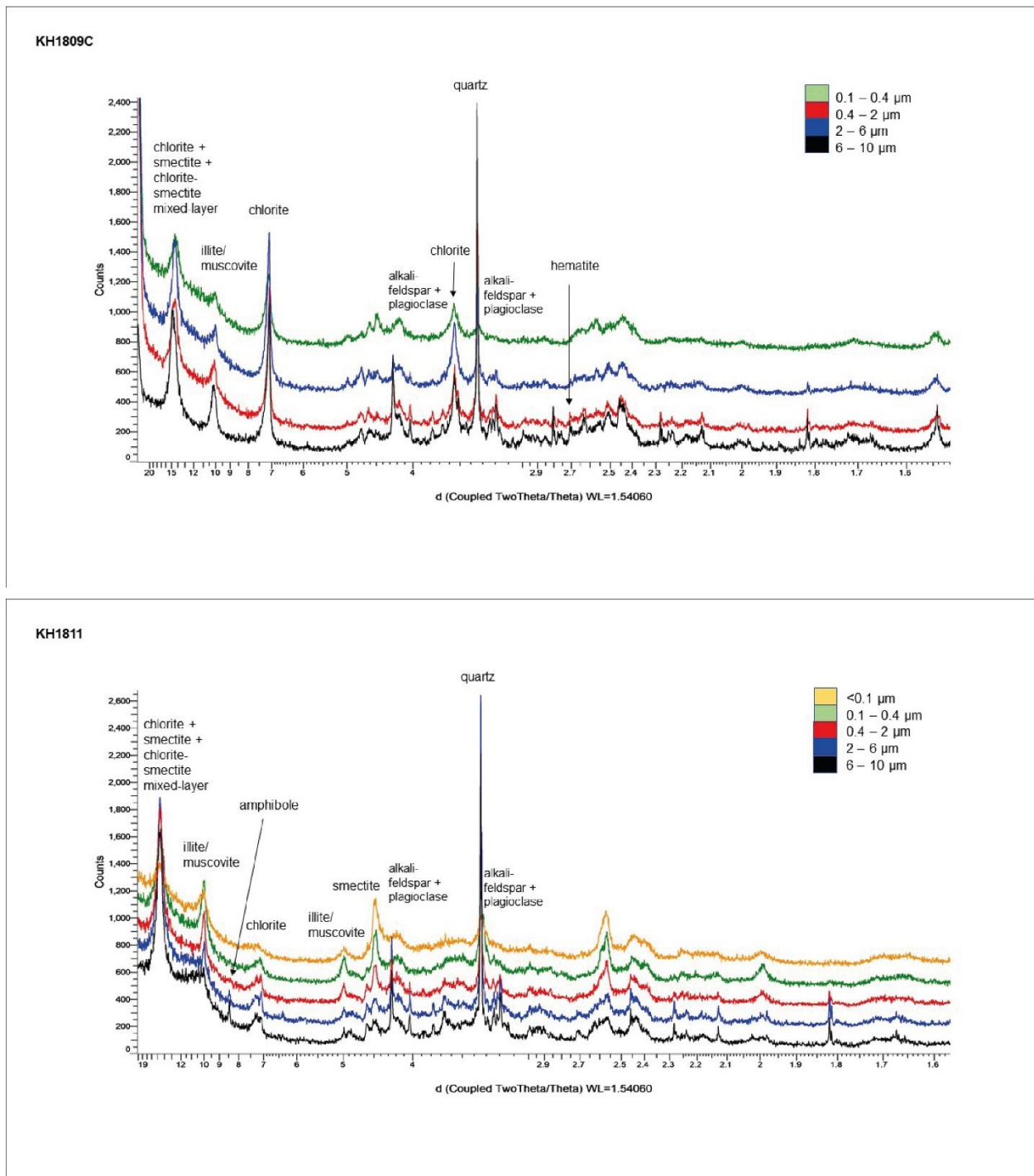
434 Based on the qualitative assessment of the peaks at 2.8 and 2.58 Å and peak shapes at 10 Å in the
435 diffractogram, it is possible to infer the crystallinity of illite/muscovite. Authigenic (1M
436 polytype) illite is characterized by a broad, poorly defined peak at 10 Å. Polytype 2M1 has a
437 characteristic peak at 2.8 Å and also shares the 2.58 Å with the 1M polytype (Grathoff & Moore,
438 1996).

439

440

Sample parameters		Identified minerals (volume fraction in %)								Refinement parameters		Illite crystallinity	
Sample ID	Size fraction [µm]	Qtz	K-fsp	Plag	Ill/musc	Ill-sm	Chl+sm+c hl-sm	amph	hem	GOF	Rwp	Standardized Kübler Index	Illite polytype
KH1811	<0.1 *				<40		60					1.03	1M
	0.1-0.4 *				50		50			2.52	19.37	0.84	1M
	0.4-2	7	5	9	31		48		?	2.12	16.63	0.54	1M
	2-6	14	10	15	14		43	4		2.3	17.63	0.42	1M
	6-10	12	11	16	14		42	5		2.37	18.16	Not possible	1M
KH1809 C	<0.1	<i>Not enough material</i>											<i>not analysed</i>
	0.1-0.4 *	2			24		74			2.19	18.45	0.77	1M
	0.4-2 *	8	5	10	17		57		3	2.2	18.17	0.62	1M
	2-6 *	19	8	15	10		44		4	2.23	18.75	0.78	2M1 likely
	6-10 *	19	11	12	9		44		5	2.56	19.62	0.82	2M1 likely

441 Table S1: Mineralogical composition determined by XRD-analysis. Abbreviations are: qtz =
442 quartz, K-fsp = alkali-feldspar, plag = plagioclase, ill/musc = illite/muscovite, chl + sm + chl+sm
443 = chlorite + smectite + chlorite-smectite mixed-layer clay, amph = amphibole, hem = hematite;
444 GOF = goodness of fit, Rwp = weighted profile factor.



445

446 Figure S3. XRD patterns (diffractograms) for samples KH1809C and KH1811, with
 447 identification of minerals.

448 S2.2 K-Ar methodology

449 Splits of approximately 1 to 3.5 milligrams of air dried, homogenized clay materials and standards
 450 were packed in weighed molybdenum envelopes, and the net mass of the aliquots was determined

451 using a Mettler Toledo XPE26DR microbalance fitted with an antistatic ionizer. The microbalance
452 has a resolution of 2 μg and a measured reproducibility of 4 μg (1σ). The clays and standards were
453 left overnight in a drying oven at $85 \pm 3^\circ\text{C}$, and then left to cool in an exicator. The molybdenum
454 envelopes were subsequently loaded into a stainless steel ultra high vacuum extraction line, and
455 baked at a maximum temperature of 120°C to eliminate excess water, while avoiding unwanted
456 $^{40}\text{Ar}^*$ loss from the samples, following the recommendations of Clauer and Chaudhuri (1995).

457 Argon was extracted from the aliquots for 20 minutes at 1400 degrees in a Pond Engineering
458 double vacuum resistance furnace. During heating, bulk sample gas was expanded directly into a
459 stainless steel vessel housing a freshly activated Titanium Sublimation Pump, to strip the sample
460 gas from a majority of reactive gases including H_2O , N, O, CO and CO_2 (O'Hanlon, 2005). Purified
461 sample gas was spiked with a known amount (approximately 2×10^{-13} moles) of pure ^{38}Ar spike
462 (Schumacher, 1975) and equilibrated for two minutes. The gas mixture was subsequently isolated
463 in a second cleanup stage and exposed for 10 minutes to two SAES GP50 getter cartridges with
464 ST101 Zr-Al alloy, one of which was kept at 350°C and one at room temperature, to remove
465 residual reactive gases including H_2 and CH_4 .

466 Argon isotopes were determined on an IsotopX NGX multicollector noble gas mass spectrometer
467 using faraday cups fitted with $10^{12} \Omega$ amplifiers, except for ^{40}Ar which was measured using a
468 faraday fitted with a $10^{11} \Omega$ amplifier. Time-zero beam intensities were measured for 30 cycles of
469 20 1-second integrations, and time-zero intensities were calculated using exponential regressions
470 back to gas inlet time. Furnace blanks were run regularly between samples, and had Ar
471 compositions comparable to atmospheric argon. Instrument mass discrimination was determined
472 within this analytical batch by a comparing a weighted mean of 50 analyses of atmospheric argon
473 ($^{40}\text{Ar}/^{36}\text{Ar} = 299.56 \pm 0.05$) with the reference value of 298.56 ± 0.31 (Lee et al., 2006). The ^{38}Ar
474 spike pipette was calibrated using GA-1550 biotite with $^{40}\text{Ar}^* = 1.342 \pm 0.007 \times 10^{-9}$ mol/g
475 (McDougall and Wellman, 2011) and HD-B1 biotite (Fuhrmann et al., 1987) with a
476 $^{40}\text{Ar}^* = 3.351 \pm 0.01 \times 10^{-10}$ mol/g (Charbit et al., 1998). The overall standard deviation of the
477 pooled spike calibrations by combined GA1550 and HD-B1 is $<0.3\%$. The accuracy of the $^{40}\text{Ar}^*$
478 determinations was monitored within run by HD-B1 biotite.

479 Potassium concentration was determined by digesting aliquots of ~ 50 mg of sample material in
480 $\text{Li}_2\text{B}_4\text{O}_7$ flux at a temperature of $1000 \pm 50^\circ\text{C}$ in palladium crucibles. The resulting glass was
481 subsequently dissolved in HNO_3 , and analysed on a Perkin Elmer Optima 4300 DV ICP-OES. 1σ
482 uncertainties depend on the sample weight and its K concentration, and are typically 1.5% relative
483 for pure mica, as determined by repeated measurements of several geological standards.

484 K-Ar ages were calculated using the ^{40}K decay constants, abundance and branching ratio of Steiger
485 and Jaeger (1977). Atmospheric argon corrections were performed using the relative abundances
486 of ^{40}Ar , ^{38}Ar and ^{36}Ar of Lee et al. (2006; $^{40}\text{Ar}/^{36}\text{Ar} = 298.56 \pm 0.31$). 1σ uncertainties were
487 estimated using the error equation for multicollector isotope dilution measurements from Halas
488 and Wojtowicz (2014) modified to consider the uncertainty on mass discrimination.

489

490 S2.3 Microprobe measurements on feldspar

491 A series of microprobe measurements for the major element chemistry were conducted to
 492 investigate the composition of feldspar present in sample KH1811. The results are presented in
 493 Table S2.

Measurement No.	Na2O	SiO2	Al2O3	MgO	TiO2	K2O	CaO	BaO	FeO	MnO	Total
1	0.3864	65.44	18.92	0	0.0535	15.4	0.0145	1.79	0.0765	0	102.0808
2	0.4414	64.61	18.55	0	0.017	15.45	0.0055	1.82	0.033	0	100.9268
3	0.2849	64.42	18.59	0	0.0462	15.46	0.0032	1.88	0.0095	0.0229	100.7166
4	0.3445	64.81	18.71	0.0205	0.095	15.5	0	1.91	0.0116	0	101.4015
5	0.197	63.63	18.41	0	0.0024	15.99	0	1.0598	0.0883	0	99.3776
6	0.3351	64.66	18.75	0	0.0827	15.4	0	2.01	0.1039	0.0042	101.3459
7	0.3158	64.83	18.68	0.0214	0.0098	15.57	0.0282	1.65	0.0253	0.0042	101.1347
8	0.4066	64.9	18.78	0.0135	0.0731	15.36	0	1.83	0.0432	0	101.4063
9	0.3094	64.48	18.79	0	0.039	15.53	0	1.83	0.0723	0	101.0507
10	0.2674	64.78	19.05	0	0	15.46	0	1.81	0.0487	0.0042	101.4202
Minimum	0.197	63.63	18.41	0	0	15.36	0	1.0598	0.0095	0	99.3775
Maximum	0.4414	65.44	19.05	0.0214	0.095	15.99	0.0282	2.01	0.1039	0.0229	102.0809
Average	0.3289	64.656	18.723	0.0055	0.0419	15.512	0.0051	1.759	0.0512	0.0036	101.0862
One sigma	0.0715	0.4577	0.1831	0.0092	0.0343	0.1794	0.0093	0.2622	0.0327	0.0071	0.7036

494

495 Table S2: Major element composition obtained for feldspar, based on spot-based analysis with
 496 microprobe. In all cases the feldspar composition is dominated by potassium, and are K-
 497 feldspars.

498

499

500

501

502 References

503 Charbit, S., Guillou, H., Turpin, L., 1998. Cross calibration of K–Ar standard minerals using an
 504 unspiked Ar measurement technique. *Chemical Geology* 150, 147–159.

505 Clauer, N., Chaudhuri, S., 1995. Clays in crustal environments. Isotope tracing and dating.
 506 Berlin, Springer-Verlag.

507 Fuhrmann, U., Lippolt, H., Hess, J.C., 1987. HD-B1 Biotite reference material for K-Ar
 508 chronometry. *Chemical Geology*, 66, 41–51

509 Hałas, S., Wójtowicz, A., 2014. Propagation of error formulas for K/Ar dating method.
 510 *Geochronometria*, 41, 202–206.

511 Lee, J.-Y., Marti, K., Severinghaus, J.P., Kawamura, K., Yoo, H.-S., Lee, J.B., Kim, J.S., 2006.
 512 A redetermination of the isotopic abundances of atmospheric Ar. *Geochimica et Cosmochimica*
 513 *Acta*, 70, 4507–4512.

- 514 McDougall, I., Wellman, P., 2011. Calibration of GA1550 biotite standard for K/Ar and 40
515 Ar/39 Ar dating. *Chemical Geology*, 280, 19–25.
- 516 O’Hanlon, J.F., 2005. A user’s guide to vacuum technology. John Wiley & Sons.
- 517 Schumacher, E., 1975. Herstellung von >99,9997% 38Argon für die 40K-40Ar Geochronologie.
518 *Chimia*, 29, 441–442.
- 519 Steiger, R.H., Jäger, E., 1977. Subcommittee on geochronology: convention on the use of
520 decay constants in geochronology and cosmochronology. *Earth and Planetary Science Letters*,
521 36, 359–362.
- 522 Warr, L.N. (2018), A new collection of clay mineral “Crystallinity” Index standards and revised
523 guidelines for the calibration of Kübler and Árkai indices. *Clay Minerals* 53, 1-12.
- 524 Warr, L.N. & Rice, A.H.N., (1994), Interlaboratory standardization and calibration of clay
525 mineral crystallinity and crystallite size data. *Journal of metamorphic Geology* 12, 141-152.
- 526